Weld World (2013) 57:73–83
DOI 10.1007/s40194-012-0008-0

RESEARCH PAPER

Influence of aluminum content on the characterization of microstructure and inclusions in high-strength steel welds

W. Vanovsek · C. Bernhard · M. Fiedler · G. Posch

Received: 9 August 2011 / Accepted: 24 July 2012 / Published online: 7 December 2012

Abstract The present study describes the methods for the characterization of the microstructure of welded joints from test welds. This comprises the analysis of the solidification microstructure (primary and secondary dendrite arm spacing) as well as the former austenite grain size and the final phase distribution. The main focus is the characterization of nonmetallic inclusions by means of SEM/EDX and light microscopy. Based on already-developed prototypes with a weld yield strength of more than 800 MPa, different kinds of inclusions and precipitates have been assessed with respect to grain refinement and the resulting impact on strength and ductility. The effect of aluminum, in the range 90 to 800 ppm, on the microstructure and the mechanical properties of high-strength steel weld metals has been studied and it has been found that at low aluminum contents good values for the tensile strength and the toughness could be obtained. The results of metallographic investigations of test welds with different alloy compositions are presented. The results indicate a significant change of the size distribution, the morphology, and the composition of the inclusions. These results are finally compared with results from literature and discussed with respect to the expected influence on the mechanical properties of the welded joint.

Keywords (IIW Thesaurus) Welding · High · Strength · Steels · Wire · Alloying additions · Inclusions

Doc. IIW-2269, recommended for publication by Commission II "Arc Welding and Filler Metals".

W. Vanovsek (✉) · C. Bernhard
Montanuniversitaet, Leoben, Austria
e-mail: wolfgang.vanovsek@unileoben.ac.at

C. Bernhard
e-mail: christian.bernhard@unileoben.ac.at

M. Fiedler
Böhler Schweißtechnik Austria GmbH, Kapfenberg, Austria
e-mail: michael.fiedler@bsga.at

G. Posch
FRONIUS International GmbH, Wels, Austria
e-mail: posch.gerhard@fronius.com

1 Introduction

The desired microstructure of advanced structural steels and high-strength steels is achieved by reducing ferrite grain size through alloying, plastic deformation, and/or low-temperature phase transformations [1–5]. However, fusion welding of these steels can lead to a change of the optimum microstructure that is obtained before welding as a result of remelting and resolidification of the base metal. By using appropriate filler metals, deterioration of the mechanical properties caused by weld-effected microstructures can be prevented. It is customary that developments of filler metal, base metal, and welding processing are performed separatly. However, welds of high-strength steels require an exact adjustment between the base metal, filler metal, and correct welding parameters for achieving optimal properties of welded joints. Therefore, it is necessary to understand the solidification process and to control the metallurgical processes which occur during welding of steels. In general, low-alloy steels undergo multiple phase transformations during solidification and subsequent cooling [6]. Depending on the cooling rate, carbon, or the substitutional alloy content, the primary solidification product will either be delta ferrite δ_{Fe}, austenite γ_{Fe}, or a mixture of both [7, 8]. Figure 1 illustrates solidification and cooling sequences that occur in a hypoperitectic or peritectic low-alloyed steel weld metal region [9, 10].

At temperatures above the liquidus temperature or during the subsequent solidification, the dissolved oxygen and nitrogen react with alloying elements to form oxidic inclusions and nitrides. When a low-alloyed steel is slowly cooled below the solidification temperature, delta ferrite will be the first phase to form [11]. In fusion welds, the delta ferrite grains reveal an anisotropic columnar morphology, with their major axes aligned in the direction of the steepest temperature gradient in the weld pool. On further cooling, austenite nucleates epitaxially at primary delta ferrite grain boundaries (Fig. 1). Subsequent growth of the austenite into the delta ferrite may then proceed by a peritectic transformation at a rate which might be controlled by diffusion of carbon in the austenite [6]. Depending on steel composition and welding conditions, the weld metal can directly solidify as austenite without any primary precipitation of delta ferrite [12]. This solidification mode has been observed during welding with covered electrodes in high-carbon steels [13]. Because of competitive growth occurring during the initial stages of the solidification process, the columnar austenite grains will have one of their <100> axes aligned in the direction of the maximum temperature gradient in the weld pool [6]. Consequently, the weld metal will develop a solidification texture which is similar to that observed during primary precipitation [14].

With a decrease in temperature to ~1,000 K, allotriomorphic alpha ferrite nucleates along the austenite grain boundaries (Fig. 1). With a further drop in temperature, the allotriomorphic ferrite grows inward toward the center of the grain. Continued decrease in temperature leads to the formation of Widmanstätten ferrite followed by acicular ferrite, bainite, and martensite [10].

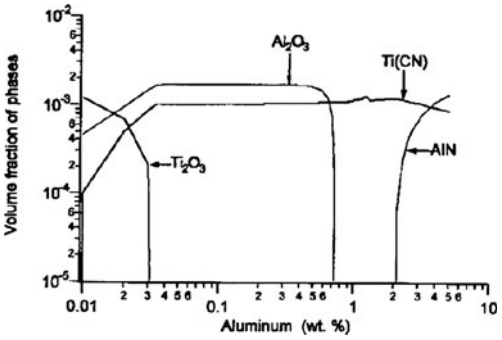

Fig. 2 Equilibrium thermodynamic calculations for low aluminum weld [28]

Bainite forms when the austenite grain size is small because nucleation predominates at the grain boundaries. Subsequent growth then swamps the interiors of the austenite grains, preventing the development of acicular ferrite [12, 15]. When the austenite grain size is large, the number density of inclusions becomes large relative to boundary nucleation sites promoting the formation of acicular ferrite at the expense of bainite (Fig. 1).

In addition to the cooling rate, nonmetallic inclusions have also an influence on grain size [16]. Grain size and the resulting microstructure of steel play an important role in the final mechanical properties. Nonmetallic inclusions can act as nucleating sites for formation of acicular ferrite during solidification and they also can promote grain refinement by inhibiting grain growth. By controlling the composition and

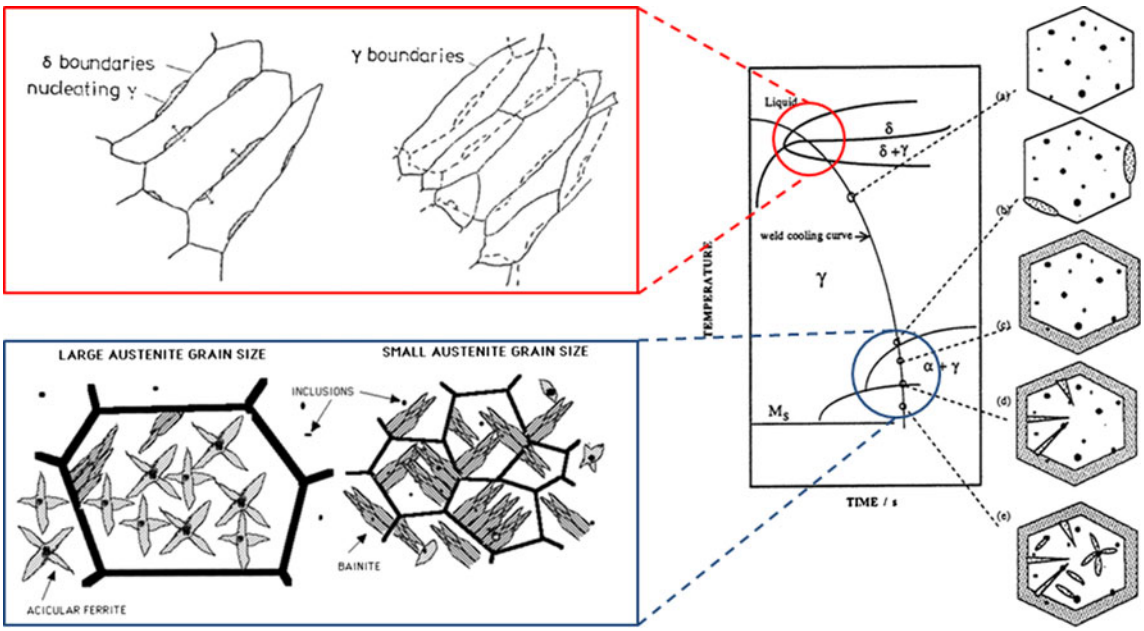

Fig. 1 Schematic illustration of inclusion formation; solidification to delta ferrite; transformation of delta ferrite to austenite; and decomposition of austenite to different alpha ferrite morphologies, including allotriomorphic ferrite, Widmanstätten ferrite, bainite, and acicular ferrite [9, 12, 15]

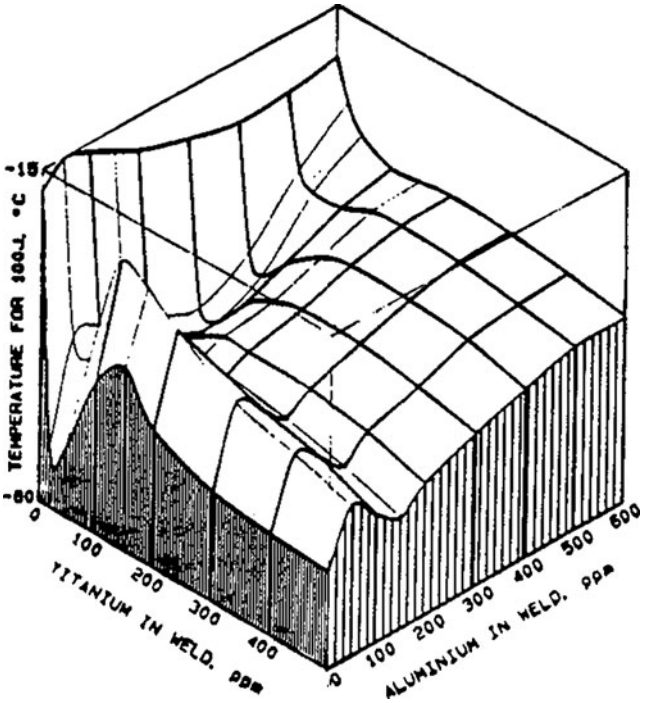

Fig. 3 Notch toughness model of the Al–Ti system [19]

size of nonmetallic inclusions in steelmaking and welding, the final product quality can be improved [17]. By the use of thermodynamic calculation, an earlier study has shown that titanium oxide inclusions will form at an aluminum content of less than 50 ppm but Al_2O_3 will form at higher aluminum contents (Fig. 2).

In another study, oxide inclusions were identified as Al_2O_3 (1–3 μm) in an Al-killed steel and as Ti–Al–(Mg)–O (0.3–0.5 μm) in Ti-killed steels. Oxide inclusion sizes in all the Ti-killed steels were smaller and inclusion densities higher than those in the Al-killed steel. Solidification structure, defined as the density of primary dendrite arms within a defined region was finer with increasing inclusion density and as a result, the solidification structure of the Ti-killed steel was finer than that of the Al-killed steel [18].

In a study of G.M. Evans [19], the combined effect of Al and Ti, in the range 5 to 500 ppm, on the microstructure and the mechanical properties of C–Mn-shielded metal arc welds has been investigated (Fig. 3). It was found that Ti, in contrast to Al, dramatically enhanced the formation of acicular ferrite and improved notch toughness. A strong interactive effect was observed, with Al at low concentrations tending to diminish the influence of Ti. Unless a critical balance was achieved with regard to the oxygen content, it was concluded that Ti be optimized at 30–40 ppm and that Al be kept as low as possible.

The present study describes the methods for the characterization of the microstructure from test welds with the aluminum content being varied between 90 and 732 ppm. The results indicate a significant change of the size distribution, the morphology, and the composition of the nonmetallic inclusions.

Table 1 Target values of the chemical composition of the weld samples, weight percent

C	Si	Mn	P	S	Cr	Mo	Ni	Ti
0.06	0.7	1.5	0.009	0.008	0.4	0.3	2	0.014

Table 2 Al and O/N content of the weld samples, ppm

Variation of the aluminum content						
Al, ppm	90	110	230	390	540	732
O, ppm	396	484	555	574	592	473
N, ppm	29	62	26	29	23	25

2 Nonmetallic inclusions

Nonmetallic oxide inclusions in steel can be classified according to their origin, their chemical composition, or the time of their formation [20].

In terms of their derivation endogenous and exogenous oxide inclusions can be distinguished. Endogenous inclusions are reaction products remaining from deoxidation. By contrast, exogenous inclusions form by subsequent reaction of the metal with oxygen. The majority of oxide inclusions in steel are endogenous inclusions.

With respect to chemical composition, oxide inclusions can be classified as follows:

- MeO: Mostly iron is partially replaced by manganese (FeO, MnO, or (Fe, Mn)O)
- Corundum: Me_2O_3 for example Al_2O_3
- Spinel: $MgO \times Al_2O_3$, $FeO \times Al_2O_3$, and $MnO \times Al_2O_3$ (galaxite)
- Silicates: $3Al_2O_3 \times 2SiO_2$ (mullite), $MnO \times SiO_2$ (rodonite), and $2MnO \times 2Al_2O_3 \times 5SiO_2$
- $CaO \times SiO_2$, $2FeO \times SiO_2$ (fayalite), and (Fe, Mn)-silicates

With the respect to the time of formation, metallic oxide inclusions can be classified as primary, secondary, or tertiary inclusions [21–23].

Table 3 Welding parameters

Current, A	Voltage, V	Weldingspeed, cm/min	Heat input per unit length, kJ/cm
250	30	56	8

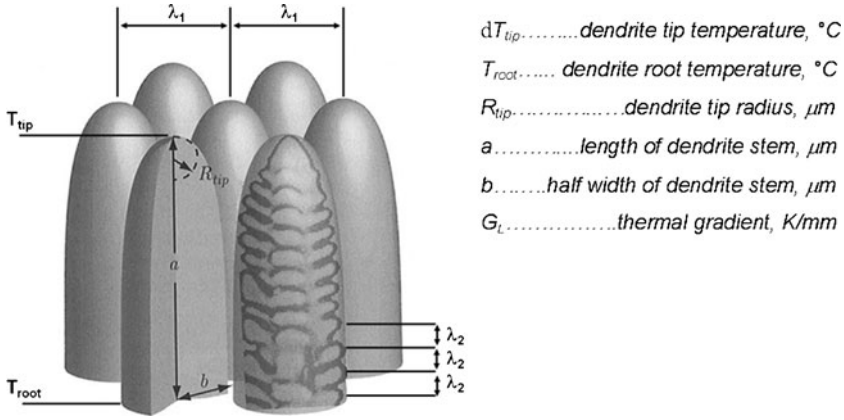

Fig. 4 Definition of primary λ_1 and secondary λ_2 dendrite arm spacing [16]

3 Materials and experimental details

Weld samples with different aluminum contents were produced. The aluminum content varied between 90 and 732 ppm. Other alloying elements were kept constant (Tables 1 and 2).

The main aim of the investigation was to establish a relation between microstructure mechanical properties. The main focus is the characterization of the nonmetallic inclusions by means of SEM/EDX and light microscopy.

Since the welding parameters have an overriding effect on the cooling rate and thus on the solidification rate, care must be taken that voltage, current, and welding speed remain constant during welding (Table 3). This ensures that every test is done with same heat input length per unit and the $t_{8,5}$ time remains constant.

3.1 Metallographic determination of primary λ_1 and secondary λ_2 dendrite arm spacing

The first step in the investigation was the assessment of the primary microstructure of the welds, the primary and secondary dendrite arm spacing were measured.

Depending upon the directional growth conditions, the dendrites (from Greek, dendron=tree) will develop arms of various orders. A dendritic form is usually characterized in terms of the primary (dendrite trunk) spacing, λ_1, and secondary (dendrite arm) spacing, λ_2 (Fig. 4). It is important to note that the value of λ_1 measured in the solidified microstructure is the same as that existing during growth, whereas the secondary spacing is significantly increased by the long contact time between the highly curved, branched structure and the melt [23].

During the further growth of the primary trunks, the secondary arms may already hit on the diffusion field of other branches of neighboring dendrites, so their growth is inhibited. Secondary arms begin to coarse and ripen. While the distance between the primary dendrite trunks at the beginning of solidification is the same as those that can be measured on the solidified microstructure the secondary dendrite arm spacing, λ_2, is subject to a ripening process. In the beginning, the secondary dendrite arm spacing is very small, but in the course of time and at a low solid fraction, an arm may remelt in support of an arm with a better growth direction by Ostwald ripening. This process continues all the way to the roots of primary dendrites, where the final dendrite arm spacing, λ_2, is reached [16, 24].

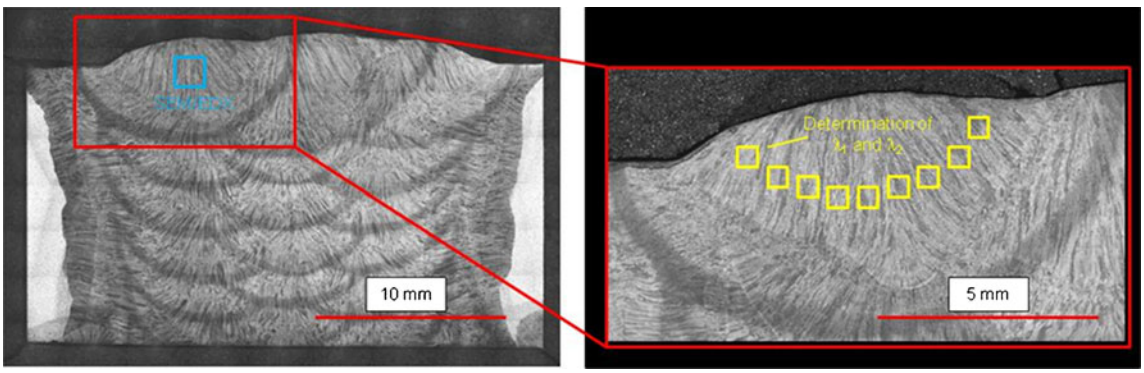

Fig. 5 Areas of metallographic investigation

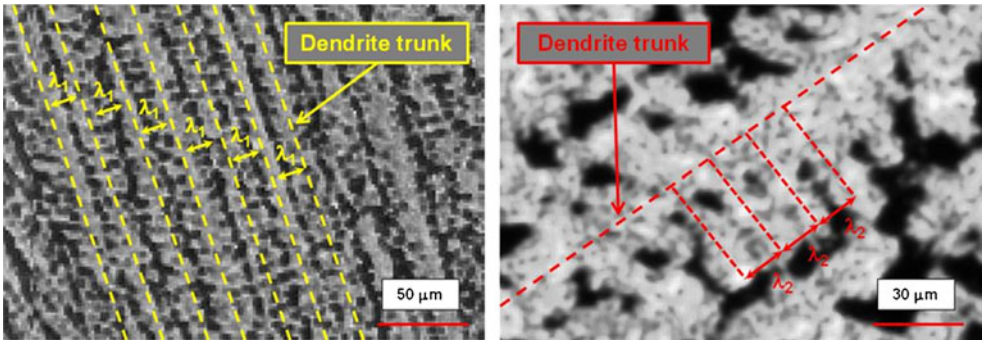

Fig. 6 Measurement of the dendrite arm spacing. **a** Primary dendrite arm spacing; **b** secondary dendrite arm spacing

It is assumed that the cell or dendrite envelope, representing the mean cross-section of the trunk and branches, can be described approximately by an ellipse. The radius of curvature of the ellipse is given by Eq. (1):

$$R_{\text{tip}} = \frac{b^2}{a} \tag{1}$$

In practical applications, the dendrite tip radius R_{tip} is not as important as the primary arm spacing λ_1 since it is very difficult to measure it directly [23]. In general, the primary arm spacing λ_1 is proportional to the half width b of the dendrite stem. In cases where the arrangement of the dendrite trunks can be represented by a simple close packed hexagonal array, the value of b is exactly equal to $\lambda_1/\sqrt{3}$ [17, 24].

Similarly, the total length of the dendrite stem, a can be calculated by considering the difference between the tip temperature T_{tip} and the root temperature T_{root} [16, 23]:

$$a = \frac{T_{\text{tip}} - T_{\text{root}}}{G_L} \tag{2}$$

The dendrite arm spacings were determined by optical microscopical examination following polishing and etching (composition of the etchant—170 ml picrid acid, 30 ml water dest., 1.7 ml HCl concentration, and 10 ml Agebon). The etching was performed in two steps at 25–30 °C. In the first step, the sample was etched for 20–30 s until the austenite grains appeared. After metallographic observation of the austenite grains the sample was further etched with the same etchant and the same etching temperature until the dendrite arms were visible.

The studied welds consist of seven layers and each layer is prepared with three weld beads. Because a weld layer consists of a cast structure, which is influenced by heat treatment when the next layer is deposited, the primary dendrite arm spacings were measured in the area of directional solidification in the last weld bead of the last weld layer of the sample (Fig. 5).

For the measurement of the primary dendrite arm spacing in the last weld bead, nine areas were selected, and in each area, 40 measurements were made. From 360 individual measurements, the average value of the primary dendrite spacing was finally determined. In the selected area the secondary dendrite arm spacing was measured. Because the secondary dendrite

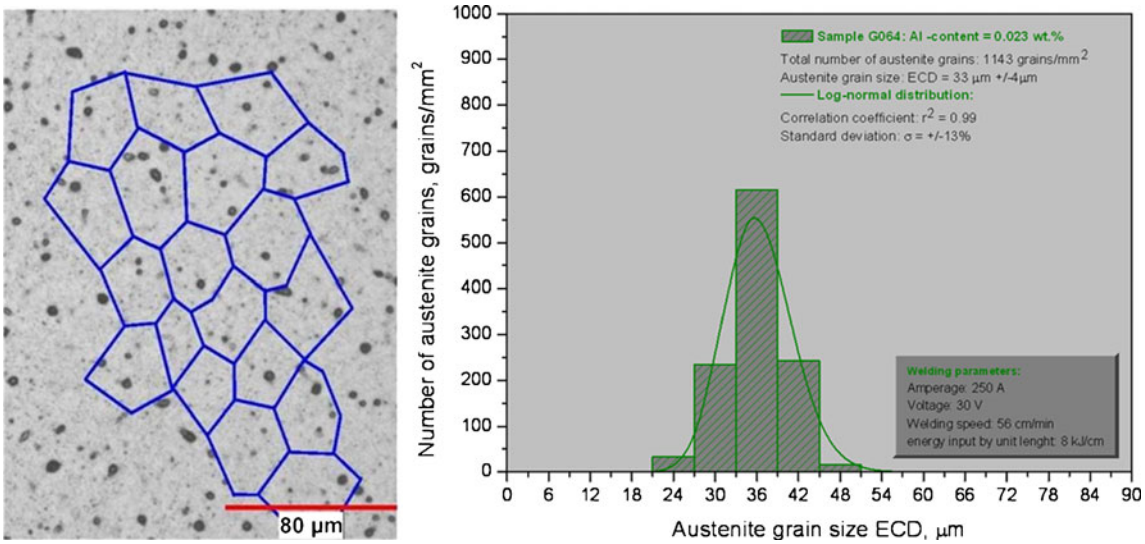

Fig. 7 Measurement of austenite grain size

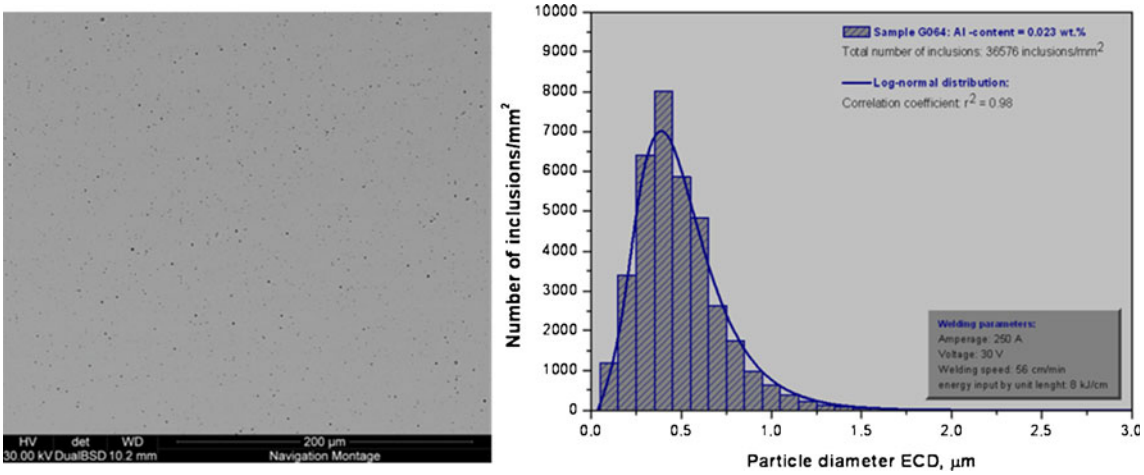

Fig. 8 Distribution of nonmetallic inclusions

spacing is much smaller at the dendrite tip the spacing was measured in middle of the dendrite trunk (Fig. 6).

3.2 Austenite grain size

A further important parameter of the microstructure is the austenite grain size. Most steel weld metals begin their solidification with the formation of δ-ferrite and in the majority of cases it is accompanied by nucleation of austenite on the δ-ferrite grain boundaries as shown in Fig. 1 [25]. The δ-ferrite grains that form on solidification are reported to have elongated or columnar structure [26, 27]. When δ-ferrite forms, two major solid-phase transformations occur on cooling to room temperature. The first occurs at high temperatures with δ-ferrite transforming to austenite approximately between 1,400 and 1,500 °C. The austenite is reported to grow from side to side across the δ-ferrite grains. It is generally not possible to clearly see the former austenite boundaries after transformation has taken place at lower temperatures [26]. In any case, the formation of austenite happens very quickly and its grain size is a very important factor, since austenite grain size has an influence on the final mechanical properties.

The measurement of the austenite grain size was also done in the last weld bead of the sample. In order to get a good result, the equivalent circle diameter (ECD) of the austenite grains was determined at six different positions on the surface. Of about 300 measured grains, the number of grains per square millimeter was determined and presented in a log-normal distribution (Fig. 7).

3.3 SEM/EDX

Nonmetallic inclusions play an important role in the metallurgy of welding. An arc-weld deposit typically contains some $10^{18} m^{-3}$ inclusions of a size greater than 0.05 µm, with a mean size of about 0.4 µm, distributed throughout the

Fig. 9 SEM/EDX analysis

SEM/EDX* analysis:

In general, all inclusion types can be detected simultaneously during the measurement. The output consists of the morphological data of every detected particle as well as its chemical composition. This picture shows the position of all inclusions classified as $MnO\text{-}SiO_2\text{-}Al_2O_3$-type inclusions in the $MnO\text{-}SiO_2\text{-}Al_2O_3$-system.

*Scanning electron microscope (SEM); Energy-dispersive X-ray spectroscopy (EDS or EDX)

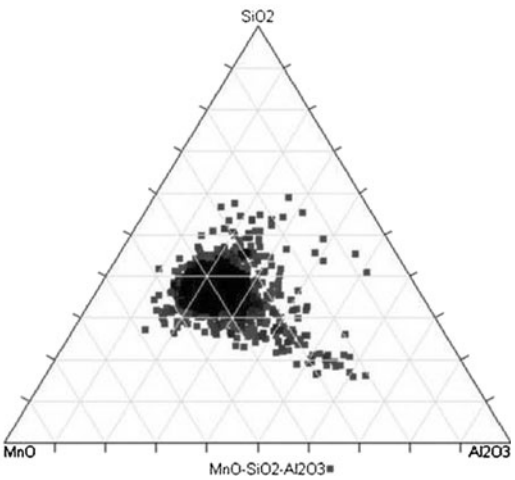

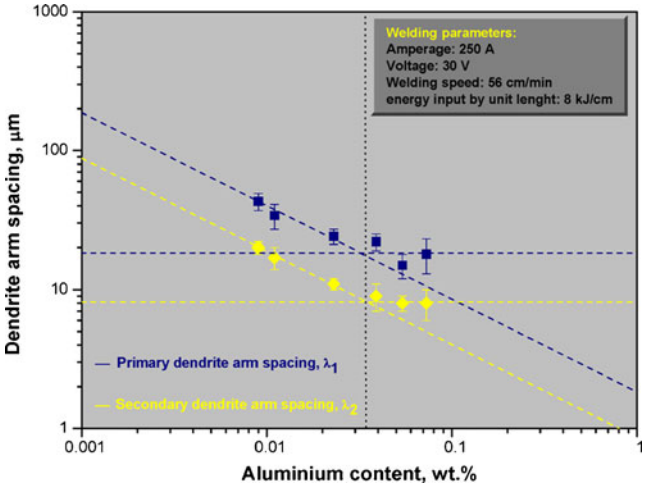

Fig. 10 Relation between dendrite arm spacing and aluminum content

microstructure. Inclusions form as oxygen in the liquid weld metal reacts with strong deoxidizing elements such as silicon, aluminum, and titanium [15]. The influence of aluminum content on the weld metal solidification is documented in the literature [18, 28]. With increasing Al_2O_3 contents in the inclusions the grain size decreases [6]. A small-grain-sized sample has a relatively large number density of grain boundary nucleation sites so bainite dominates the microstructure, whereas a relatively large number density of intragranular nucleation sites leads to microstructure consisting predominantly of acicular ferrite [15].

SEM/EDX analysis was done in all samples at the same position (Fig. 5). After the ECD of the inclusions was measured and the inclusion size distribution was determined (Fig. 8), inclusions were classified as shown in Fig. 9.

4 Results

With an increase in aluminum content, the primary and secondary dendrite spacing decrease as shown in Fig. 10. The

Table 4 Comparison of calculated and measured values of λ_2

Al content, ppm	λ_2 (measurement), µm	λ_2 (calculation), µm	Difference between measurement and claculation, µm
90	20	24	4
110	17	16	1
230	11	13	2
390	9	11	2
540	8	9	1
732	8	12	3

Table 5 Austenite gain size as function of aluminum content

Al content, ppm	Austenite grain size, µm	Standard deviation of the measurement, µm
90	26	3
110	28	6
230	33	4
390	27	4
540	24	3
732	23	2

observed relationship between dendrite arm spacing and the aluminum content is also described in the literature [29]. For the calculation of λ_2 the local solidification time is required, which can be calculated by Eq. 3 [6]. The dependence of secondary dendrite arm spacing on the alloy content is for example described by Cabrera-Marerro et al. in Eq. 4 [29]. The equation shows that the secondary dendrite arm spacing decreases with increasing aluminum content. The necessary temperatures T_m, T_{root}, and T_{tip} and the thermal conductivity are calculated by the IDS software [30]. Using a net arc power of 6,000 W and a welding speed of 0.0094 m/s, the calculation was done for six aluminum contents.

$$t_f = \frac{\Delta T^*}{2\pi\lambda (T_m - T_0)^2}(q_0/v), [s] \quad (3)$$

$$\lambda_2 = t_f^{1/3} \cdot [70(wt\%\,C) + 50(wt\%\,Si) - 0.755(wt\,Ni) - 3042(wt\%\,Cr)], \quad [\text{micrometer}] \quad (4)$$

t_f Local solidification time (second)
T_m Melting point (degrees Celsius or kelvin)

Table 6 SEM analysis: comparsion of inclusion size with the Al/O ratio

Al an O content of the weld sample			Number of non metallic inclusions	
Al content, ppm	O content, ppm	Al/O ratio, $\times 10^{-3}$	(ECD: 1–3 µm), parts/mm^2	Total number of inclusions, parts/mm^2
90	396	227	815	25,759
110	484	227	252	34,755
230	555	414	934	36,576
390	574	679	1,018	28,482
540	592	912	1,112	24,747
732	473	1,548	1,397	22,926

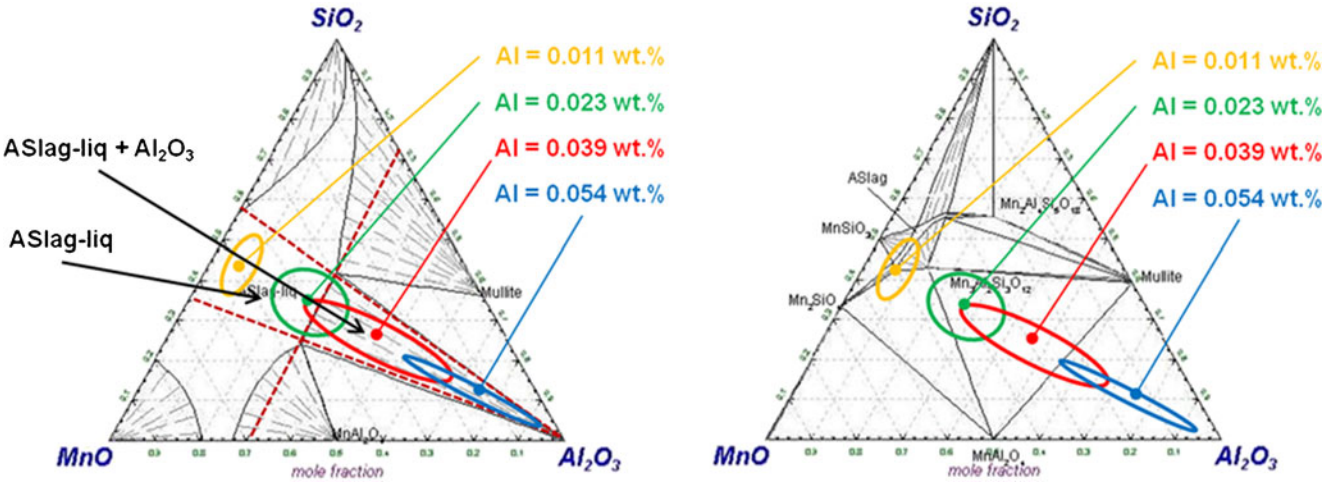

Fig. 11 Inclusion types at different aluminum content of the weld metal superimposed on the $MnO–SiO_2–Al_2O_3$ system, calculated by FACTSage 6.2. **a** $MnO–SiO_2–Al_2O_3$: 1600 °C; **b** $MnO–SiO_2–Al_2O_3$: 1150 °C

T_{root}	Dendrite root temperature (degrees Celsius or kelvin)
T_{tip}	Dendrite tip temperature (degrees Celsius or kelvin)
ΔT^*	Temperature difference between tip and root of dendrite (kelvin)
λ	Thermal conductivity (watts per meter kelvin)
q_0	Net arc power (watts)
v	Welding speed (meter per second)

It can be seen in Table 4 that the calculation and measured values are in good agreement. The difference between the measured values and the calculated values is approximately the same as the standard deviation of the measured values.

Table 5 shows that the diameter of the austenite grains increases between an aluminum content of 90–230 ppm and decrease again at higher aluminum contents.

Table 6 shows that the number of inclusions with a diameter between 1 and 3 μm is proportional to the Al/O ratio. The total number of all detected inclusions reaches a maximum at an aluminum content between 110 and 230 ppm.

The inclusions with a diameter of 1–3 μm were classified by means SEM/EDX analysis as $MnO–SiO_2–Al_2O_3$ and $MnO–SiO_2–TiO_2$ inclusions (Figs. 11 and 12).

It follows from Fig. 13 that the fraction of Al_2O_3 in the $MnO–SiO_2–Al_2O_3$-type inclusions increases until an Al/O mass ratio of 1.13 is reached [6]. Aluminum is a stronger oxidizing agent than titanium so it is expected that Al_2O_3 forms first and binds the oxygen. A thermodynamic calculation which was done by the commercial software FACTSage 6.2 shows that the $MnO–SiO_2–Al_2O_3$ inclusions form at high temperature whereas the $MnO–SiO_2–TiO_2$ inclusions

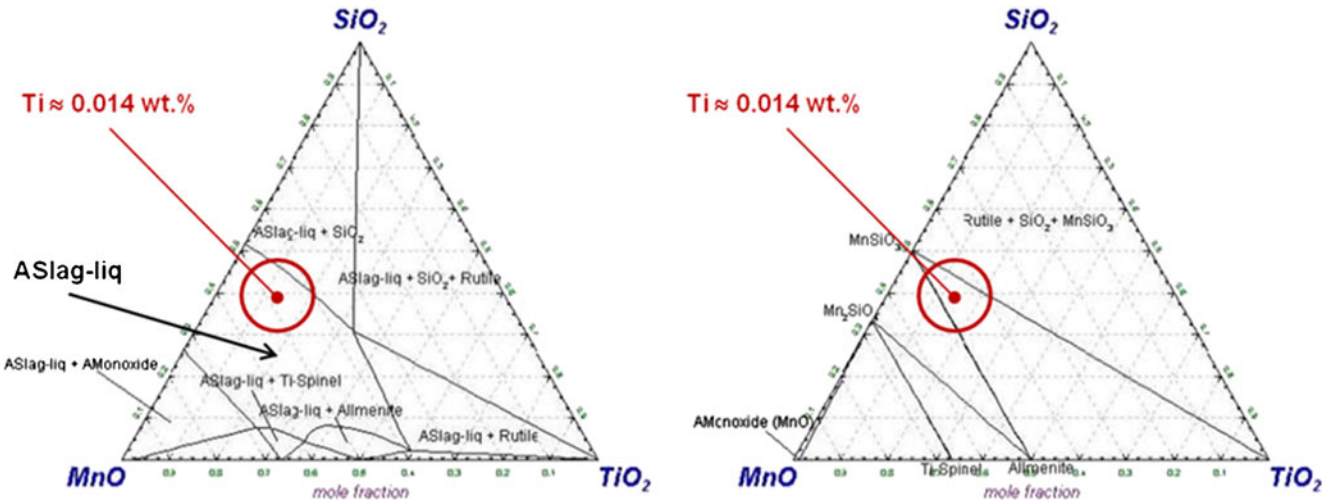

Fig. 12 Inclusion types at different aluminum content of the weld metal superimposed on the $MnO–SiO_2–TiO_2$–system, calculated by FACTSage 6.2. **a** $MnO–SiO_2–TiO_2$: 1400 °C, $p(O_2)=10^{-5}$ atm; **b** $MnO–SiO_2–TiO_2$: 1200 °C, $p(O_2)=10^{-5}$ atm

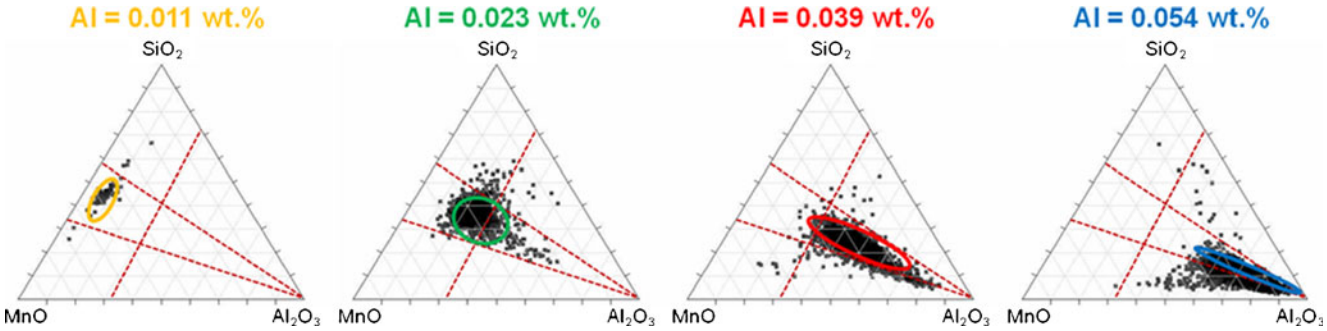

Fig. 13 Inclusion composition of $MnO–SiO_2–Al_2O_3$

form at lower temperatures. The $MnO–SiO_2–TiO_2$ inclusions have always the same position in the phase diagram, but the number of these inclusions decreases with an increase in aluminum content (Fig. 14).

The results of this study have showed that a very low Al content has a positive effect on the mechanical properties of the weld metal in agreement with earlier studies [28].

Toughness reached an optimal value at an Al content of 150 ppm and a Ti content of 150 ppm. Although the tensile strength reached in that area a local minimum, the value of the tensile strength is quite high in relation to the toughness (Fig. 15). This result is in agreement with the study of G.M. Evans. In this study, the transition temperature, the tensile strength, and the impact energy was determined (Fig. 3) [19]. The toughness also reached its optimal value at an Al content of 150 ppm and a Ti content of 150 ppm.

5 Conclusions

The present study describes the methods for the characterization of the microstructure of welded joints from test welds. This comprises the analysis of the solidification microstructure (primary and secondary dendrite arm spacing) as well as the former austenite grain size and the final phase distribution. The main focus was the characterization of the nonmetallic inclusions by means of SEM/EDX and light microscopy. The aluminum content has been varied between 90 and 732 ppm with a constant basic weld composition, whereas the welding parameters have been kept constant.

The main results are as follows.

1. With an increase in aluminum content, the primary and the secondary dendrite arm spacings decrease. The diameter of the austenite grains increases between an aluminum content of 90–230 ppm, but decrease again at higher aluminum content.
2. The number of inclusions with a diameter between 1 and 3 μm is proportional to the Al/O ratio. The total number of all detected inclusions reaches a maximum at an aluminum content between 110 and 230 ppm.

The inclusions with a diameter of 1–3 μm were identified by means SEM/EDX analysis as $MnO–SiO_2–Al_2O_3$ and $MnO–SiO_2–TiO_2$–type inclusions.

3. As described in the literature, the content of Al_2O_3 in the $MnO–SiO_2–Al_2O_3$ inclusions increases until an Al/O ratio of 1.13 is reached. Thermodynamic calculation showed that the $MnO–SiO_2–Al_2O_3$ inclusions form at high temperature whereas the $MnO–SiO_2–TiO_2$ inclusions form at lower temperatures. The $MnO–SiO_2–TiO_2$ inclusions have always the same position in the phase diagram, but the number of these inclusions decreases with higher aluminum contents.

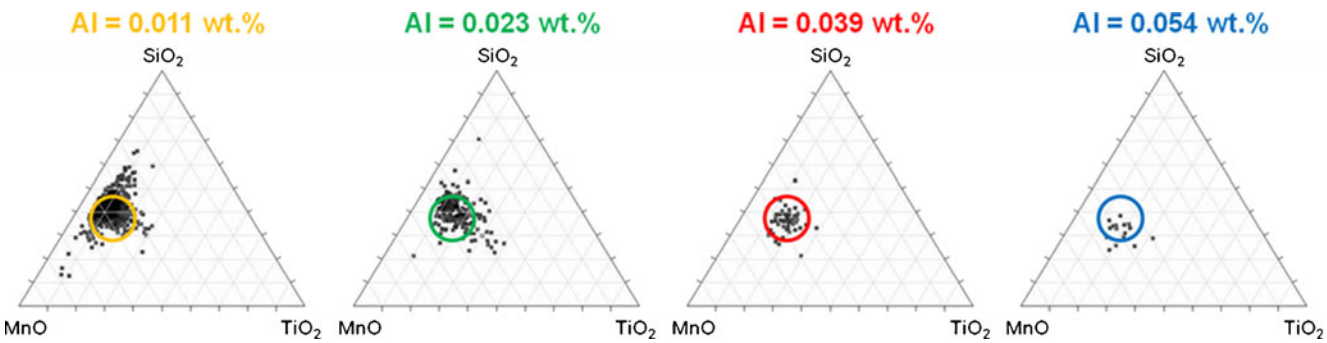

Fig. 14 Inclusion composition of $MnO–SiO_2–TiO_2$

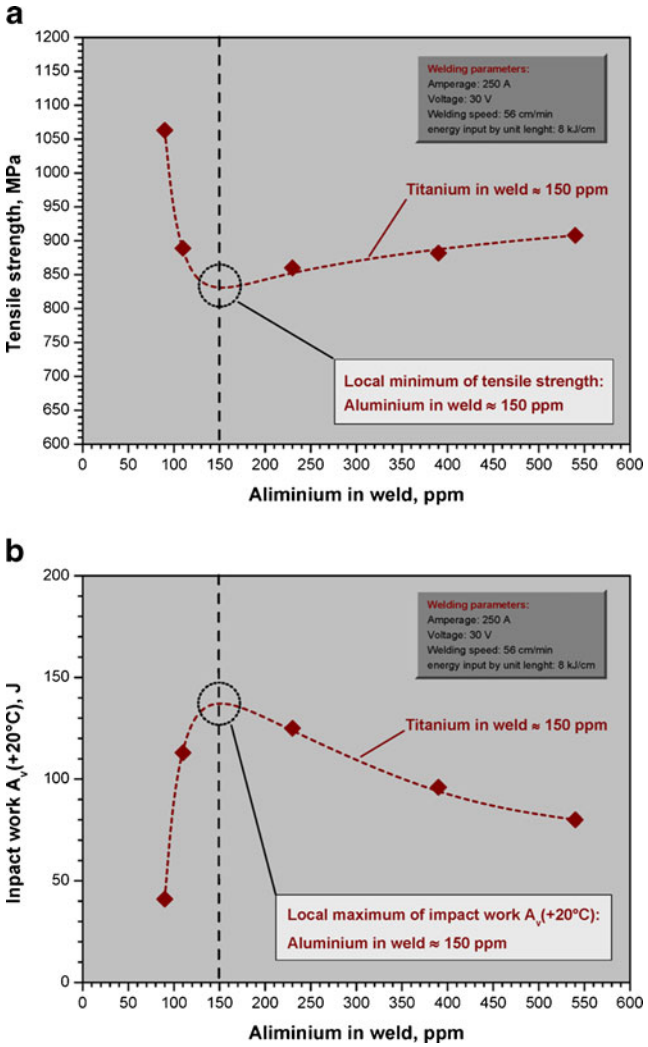

Fig. 15 Relation between tensile strength, impact work, and aluminum content. **a** Tensile strength; **b** impact work

4. At low aluminum contents, good values for the tensile strength and the toughness were attained. The toughness reached an optimal value at an aluminum content of 150 ppm and a titanium content of 150 ppm, in agreement with a study of G.M. Evans [19].

Acknowledgments The investigations presented were supported by the Böhler Schweißtechnik Austria GmbH, the Voestalpine AG and the Austrian Research Promotion Agency (FFG). Special thanks are given to all the industry partners and project partners for the support.

References

1. Belyakov A, Sakai Y, Hara T, Kimura Y, Tsuzaki K (2001) Thermal stability of ultra fine-grained steel containing dispersed oxides. Scr Mater 45(10):1213–1219
2. Takaki S, Kawasaki K, Kimura Y (2001) Mechanical properties of ultra fine grained steels. J Mater Process Technol 117(3):359–363
3. Caballero FG, Bhadeshia HKDH, Mawella KJA, Jones DG, Brown P (2002) Very strong low temperature bainite. Mater Sci Technol 18(3):279–284
4. Ouchi C (2001) Development of steel plates by intensive use of TMCP and direct quenching processes. ISIJ Int 41(6):542–553
5. Ali A, Bhadeshia HKDH (1991) Microstructure of high strength steel refined with intragranularly nucleated Widmanstätten ferrite. Mater Sci Technol 7(10):895–903
6. Grong Ø (1997) Metallurgical modelling of welding, 2nd edn. The Institute of Materials, Minerals and Mining, Cambridge
7. Frederikson H (1976) The mechanism of the peritectic reaction in iron-base alloys. Mater Sci Technol 10(3):77–86
8. Frederikson H, Stjerndahl J (1982) Solidification of iron-base alloys. Mater Sci Technol 10(12):575–585
9. Babu SS 1991 Acicular ferrite and bainite in Fe-Cr-C weld deposits. Ph.D. Thesis, University of Cambridge
10. Babu SS, David SA (2002) Inclusion formation and microstructure evolution in low alloy steel welds. ISIJ Int 42(12):1344–1353
11. Pottore NS, Garcia CI, Hiejlen J (1991) Interrupted and isothermal solidification studies of low and medium carbon steels. Metall Mater Trans A 22(8):1871–1880
12. Widgery DJ 1974 Deoxidation practice and the toughness of mild steel weld metal. Ph.D. Thesis, University of Cambridge
13. Sugden AAB, Bhadeishia HKDK (1988) The nonuniform distribution of inclusions in low-alloy steel weld deposits. Metall Mater Trans A 19(3):669–674
14. Kluken AO, Grong Ø, Hjielen J (1991) The origin of transformation textures in steel weld metals containing acicular ferrite. Metall Mater Trans A 22(3):657–663
15. Bhadeshia HKDH (2001) Bainite in steels, 2nd edn. The Institute of Materials, Minerals and Mining, Cambridge
16. Dantzig JA, Rappaz M (2009) Solidification, 1st edn. EPLF Press, Lausanne
17. Kiviö M, Holappa L, Iung T (2010) Addition of dispersoid titanium oxide inclusions in steel and their influence on grain refinement. Metall Mater Trans B 41(6):1194–1204
18. Kikuchi N, Nabeshima S, Kishimoto Y, Matsushita T, Sridhar S (2002) Effect of Ti de-oxidation on solidification and post-solidification microstructure in low carbon high manganese steel. ISIJ Int 47(9):1255–1264
19. Evans GM (1993) Microstructure and properties of ferritic steel welds containing Al and Ti. IIW Doc. II-A-901-93
20. Ovtchinnikov S 2002 Kontrollierte Erstarrung und Einschlussbildung bei der Desoxidation von hochreinen Stahlschmelzen (Controlled solidification and inclusion formation during deoxidation of high purity steel melts). Ph.D. Thesis, University of Freiberg (in German)
21. Plöckinger E, Straube H 1964 Die Desoxidation, Die physikalische Chemie der Eisen und Stahlerzeugung (The deoxidation, the physical chemistry of iron and steel production). Verlag Stahleisen, Düsseldorf pp. 303–349. (in German)
22. Javoiskij VI 1969 Theorie der Stahlerzeugung (Theory of steel production). Deutscher Verlag für Grundstoffindustrie, Leipzig (in German)
23. Kurz W, Fisher DJ (1998) Fundamentals of solidification, 4th edn. Trans Tech Publications Ltd, Zürich
24. Glicksman ME, Voorhees PW (1984) Ostwald ripening and relaxation in dendritic structures. Metall Mater Trans A 15(6):995–1001
25. Keehan E (2004) Effect of microstucture mechanical properties of high strength steel weld metals. Ph.D. Thesis, Göteborg University
26. Svensson LE (1994) Control of microstructure and properties in steel arc welds. CRC Press, Inc

27. Bhadeshia HKDH, Svensson LE, Gretoft B (1986) The austenite grain structure of low-alloy steel weld deposits. J Mater Sci 21 (11):3947–3951
28. Quintina MA, McLaine J, Babu SS, and David SA (2001) Inclusion formation in self-shielded flux cored arc welds. Welding Research Supplement pp. 98–105
29. Cabrera-Marrero JM, Carreño-Galindo V, Morales RD, Chávez-Alcalá F (1998) Macro–micro modeling of the dentritic microstructure of steel billets processed by continuous casting. ISIJ Int 38(8):812–821
30. Miettinen J (1992) Mathematical simulation of interdendritic solidification of low-alloyed and stainless steels. Metall Mater Trans A 23(4):1155–1170